

Comparison of four boundary conditions for the fluid-hydrogel interface

Zelai Xu ¹, Jiaqi Zhang ², Yuan-Nan Young ³, Pengtao Yue ⁴, and James J. Feng ^{1,5}

¹*Department of Chemical and Biological Engineering, University of British Columbia, Vancouver, British Columbia, Canada V6T 1Z3*

²*School of Mathematical and Statistical Sciences, Clemson University, Clemson, South Carolina 29634, USA*

³*Department of Mathematical Sciences, New Jersey Institute of Technology, Newark, New Jersey 07102, USA*

⁴*Department of Mathematics, Virginia Tech, Blacksburg, Virginia 24061, USA*

⁵*Department of Mathematics, University of British Columbia, Vancouver, British Columbia, Canada V6T 1Z2*



(Received 9 December 2021; accepted 13 September 2022; published 21 September 2022)

In adopting a poroelastic model for a hydrogel, one views its constituent fluid and solid phases as interpenetrating continua, thereby erasing the pore-scale geometry. This gives rise to the need for additional boundary conditions (BCs) at the interface between a hydrogel and a clear fluid to supplement the momentum equations for the fluid and solid phases in the hydrogel. Using a thermodynamic argument on energy dissipation, we propose three sets of BCs for the gel-fluid interface that link the normal and tangential velocity jumps across the interface to the normal and tangential stresses on either side of the interface. Using several flow problems—one-dimensional compression, two-layer Couette and Poiseuille shear flows, and deformation of a gel particle by a planar extension flow—as tests, we compare the predictions of these three BCs with that of a previously proposed BC. Some differences are stark and reveal flaws in certain BCs. Others are subtler and will require quantitative experimental data for validation. Based on these results, we recommend one set of BCs over the other three for computing the flow and deformation of hydrogels in contact with a clear fluid. In addition, we suggest benchmark experiments to validate the BCs and our recommendation.

DOI: [10.1103/PhysRevFluids.7.093301](https://doi.org/10.1103/PhysRevFluids.7.093301)

I. INTRODUCTION

Hydrogels are finding increasing use in biomicrofluidics. In organ-on-chip devices, for example, hydrogels often serve as the scaffold and carrier for biological cells [1]. The gels are typically exposed to a perfusing liquid stream that supplies nutrients and biochemical factors to the cells [2]. This has given importance to the mechanics of fluid-gel interfaces, and especially the boundary condition (BC) on such interfaces.

In a microstructural view, the hydrogel consists of an elastic skeleton of crosslinked polymer chains and an aqueous solvent. On such a microscopic scale, therefore, one could strive to represent the geometry of individual pores and impose the no-slip BC appropriate for fluid-solid boundaries. For large-scale hydrodynamic problems, however, such a microstructural approach is not feasible, and a coarse-grained description is more appropriate. The poroelastic model is one such model based on mixture theory, treating the solvent and skeletal phases as interpenetrating effective continua occupying certain volume fractions at each spatial point [3–5]. Thus, separate momentum equations have to be posed for each phase in the gel. Consequently, additional BCs are required at the interface between the gel and a clear solvent to specify the momentum exchange between the clear fluid outside the gel and the fluid and solid phases inside the gel.

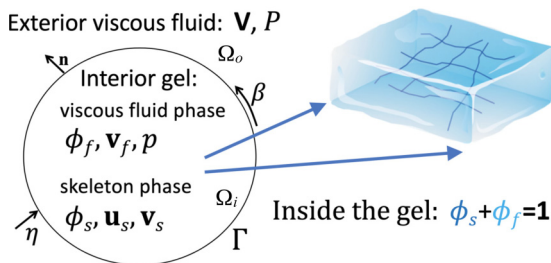


FIG. 1. A schematic for the fluid-hydrogel two-phase system, with \mathbf{n} being the outward normal vector to the gel domain, and η and β being the permeability and slip coefficients to be defined in Sec. II B.

This BC problem for hydrogels is closely related to that for rigid porous mediums, a long-standing problem in the fluid mechanics literature [6–9]. The two essential questions concern the velocity jump and stress jump across the interface, and various proposals have been made [10–13]. Based on a careful review of prior studies in porous medium, Minale [14,15] developed a set of BCs that amount to continuity of the velocity across the gel-fluid interface and a traction partition scheme that relates the fluid stress in the porous medium to the stress of the external fluid flow.

For hydrogels, an additional factor is the elastic deformation of the solid skeleton. Thus, the motion and stress of the solid phase must be included in the velocity and stress jumps at the gel-fluid interface. Toward this end, Young *et al.* [16,17] used an energy-dissipation argument to suggest thermodynamically consistent BCs. By writing the interfacial dissipation as a surface integral of the inner product of various pairs of velocity jumps and stress jumps, they proposed proportionality between the two to ensure non-negative entropy production. This procedure yields BCs that are sufficient but not necessary for satisfying the second law of thermodynamics, and Feng and Young [17] compared the predictions of two such BCs, termed BC1 and BC2, with that of Minale [15] in a one-dimensional (1D) two-layer shear flow driven by a moving plate. Interestingly, BC1 and BC2 approach essentially the same steady Darcy-flow limit when the viscous stress inside the gel becomes small. Thus, the BCs should be tested and compared in more complex fluid problems, e.g., in multidimensions, with time-dependency or with a strong viscous stress in the gel.

The current paper undertakes such tests using analytical and numerical solutions of four flow problems: 1D compression of a gel layer by a normal fluid stream, steady and oscillatory two-layer Couette flows with a clear fluid layer atop a hydrogel layer, steady two-layer Poiseuille shear flows, and the deformation of a gel particle at the stagnation point of a 2D planar extensional flow. Aside from BC1 and BC2, we propose a boundary condition BC3 using the same dissipation argument of Young *et al.* [16,17]. Along with another boundary condition BCM, generalized from that of Minale [15], the four sets of BCs are compared in the test flows to highlight their differences. BC2 emerges as the most attractive of the four. Our theoretical comparison and recommendation should be validated by future experiments to determine which BCs more faithfully represent the true physics at the interface between a fluid and a hydrogel.

II. THEORETICAL FORMULATION

A. Governing equation

The physical system consists of a hydrogel domain Ω_i and a clear fluid domain Ω_o , separated by an interface Γ (Fig. 1). The hydrogel is treated as a poroelastic medium composed of a solid skeleton and an interstitial fluid that is the same as the clear fluid outside. The fluid and solid volume fractions ϕ_f and ϕ_s satisfy $\phi_f + \phi_s = 1$.

For the clear fluid in Ω_o , inertia is negligible in typical microfluidic applications thanks to small spatial dimensions and slow flow. Thus, the flow obeys the incompressible Stokes equation:

$$\nabla \cdot \mathbf{V} = 0, \quad (1)$$

$$\nabla \cdot (\boldsymbol{\Sigma} - P\mathbf{I}) = 0, \quad (2)$$

where \mathbf{V} and P denote velocity and pressure of the fluid and $\boldsymbol{\Sigma} = \mu[\nabla\mathbf{V} + (\nabla\mathbf{V})^T]$ is the viscous stress tensor, μ being the viscosity.

In the hydrogel domain Ω_i , we define *intrinsic phase-averaged* fluid velocity \mathbf{v}_f and solid velocity \mathbf{v}_s over the fractional volumes containing only the fluid and the solid phase, respectively [10,11,15]. Due to continuity of each phase, the volume fractions satisfy the following equations:

$$\frac{\partial \phi_f}{\partial t} + \nabla \cdot (\phi_f \mathbf{v}_f) = 0, \quad (3)$$

$$\frac{\partial \phi_s}{\partial t} + \nabla \cdot (\phi_s \mathbf{v}_s) = 0. \quad (4)$$

Summing the two, we obtain a divergence-free condition for the composite velocity:

$$\nabla \cdot (\phi_f \mathbf{v}_f + \phi_s \mathbf{v}_s) = 0 \quad (5)$$

Each phase satisfies its own momentum equation:

$$\nabla \cdot (\phi_f \boldsymbol{\sigma}_f) - \phi_f \nabla p + \mathcal{F}^{s \rightarrow f} = 0, \quad (6)$$

$$\nabla \cdot (\phi_s \boldsymbol{\sigma}_s) - \phi_s \nabla p + \mathcal{F}^{f \rightarrow s} = 0, \quad (7)$$

where $\boldsymbol{\sigma}_f$ and $\boldsymbol{\sigma}_s$ are the fluid and solid stress tensors and p is pressure. The Darcy drag $\mathcal{F}^{s \rightarrow f}$ or $\mathcal{F}^{f \rightarrow s}$ is given by

$$\mathcal{F}^{s \rightarrow f} = -\mathcal{F}^{f \rightarrow s} = \xi \phi_f \phi_s (\mathbf{v}_s - \mathbf{v}_f), \quad (8)$$

with a constant drag coefficient ξ . The viscous stress of the fluid phase is $\boldsymbol{\sigma}_f = \mu_e[\nabla\mathbf{v}_f + (\nabla\mathbf{v}_f)^T]$, where μ_e is the effective viscosity [12]. This stress appears in the Brinkman equation but not in Darcy's law, and will be called the Brinkman stress. The solid velocity \mathbf{v}_s is related to the solid displacement \mathbf{u}_s by $\mathbf{v}_s = d\mathbf{u}_s/dt$. For the solid stress $\boldsymbol{\sigma}_s$, we adopt the linear elasticity model:

$$\boldsymbol{\sigma}_s = 2\mu_s \mathbf{E} + \lambda_s \text{tr}(\mathbf{E})\mathbf{I}, \quad (9)$$

where μ_s and λ_s are the Lamé constants of the solid skeletal phase, and $\mathbf{E} = [\nabla\mathbf{u}_s + (\nabla\mathbf{u}_s)^T]/2$ is the linear strain tensor. Hyperelastic models can also be used, as in Li *et al.* [18], but the linear model affords simplicity and ease of comparing the BCs in the current context. As the BCs will be expressed in terms of the stress tensors, a different constitutive equation for the solid network will not change the form of the BCs.

B. Boundary conditions

Based on the kinematics and continuity of fluid flow and a traction balance on the interface, one can write the following three general BCs:

$$\mathbf{n} \cdot \mathbf{v}_s = v_\Gamma, \quad (10)$$

$$\mathbf{n} \cdot (\mathbf{V} - \mathbf{v}_s) = \phi_f \mathbf{n} \cdot (\mathbf{v}_f - \mathbf{v}_s), \quad (11)$$

$$\mathbf{n} \cdot (\boldsymbol{\Sigma} - P\mathbf{I}) = \mathbf{n} \cdot (\phi_s \boldsymbol{\sigma}_s + \phi_f \boldsymbol{\sigma}_f - p\mathbf{I}), \quad (12)$$

where \mathbf{n} is the outward unit normal vector on the hydrogel surface and v_Γ is the normal velocity of the interface. Equation (10) is a kinematic condition for interfacial movement and Eq. (11) represents continuity of the fluid flow across the interface. Equation (12) balances the tractions on both sides of the interface, with interfacial tension being neglected for simplicity. These need to be supplemented by additional BCs that specify the interfacial velocity jumps. Young *et al.* [16,17] showed that such BCs can be proposed based on the second law of thermodynamics. Absent external energy input and work, the system's energy spontaneously dissipates. Multiplying Eqs. (2), (6), and (7), respectively, by \mathbf{V} , \mathbf{v}_f , and \mathbf{v}_s , integrating over their respective domains, and summing up the three products, we can identify an interfacial dissipation [16]:

$$I_\Gamma = \int_\Gamma [-\mathbf{V} \cdot (\boldsymbol{\Sigma} - p\mathbf{I}) + \mathbf{v}_f \cdot (\phi_f \boldsymbol{\sigma}_f - \phi_f p\mathbf{I}) + \mathbf{v}_s \cdot (\phi_s \boldsymbol{\sigma}_s - \phi_s p\mathbf{I})] \cdot \mathbf{n} ds. \quad (13)$$

The energy dissipation principle requires $I_\Gamma \leq 0$. Young *et al.* [16,17] used different relative velocities to derive two different sets of BCs that ensure positive entropy production. In the following, we will adopt more general notations to illustrate the generality of this procedure and then derive three sets of BCs as special cases. Introducing a reference velocity $\tilde{\mathbf{v}}$, we can express the dissipation rate I_Γ in terms of the velocity differences from $\tilde{\mathbf{v}}$. With the continuity condition Eq. (11) and the traction balance condition Eq. (12), we rewrite Eq. (13) as

$$I_\Gamma = \int_\Gamma [\phi_s (\mathbf{v}_s - \tilde{\mathbf{v}})_\perp \cdot (\boldsymbol{\sigma}_s - p\mathbf{I} - \boldsymbol{\Sigma} + p\mathbf{I}) + \phi_f (\mathbf{v}_f - \tilde{\mathbf{v}})_\perp \cdot (\boldsymbol{\sigma}_f - p\mathbf{I} - \boldsymbol{\Sigma} + p\mathbf{I}) - (\mathbf{V} - \tilde{\mathbf{v}})_\parallel \cdot \boldsymbol{\Sigma} + \phi_s (\mathbf{v}_s - \tilde{\mathbf{v}})_\parallel \cdot \boldsymbol{\sigma}_s + \phi_f (\mathbf{v}_f - \tilde{\mathbf{v}})_\parallel \cdot \boldsymbol{\sigma}_f] \cdot \mathbf{n} ds, \quad (14)$$

where the subscripts \perp and \parallel indicate velocity components normal and tangential to the interface. Note that the dissipation consists of products between various velocity jumps and tractions. Following a procedure in irreversible thermodynamics [19], we assume the velocity jumps to be proportional to the corresponding tractions, thus making all such terms quadratic and ensuring $I_\Gamma \leq 0$.

Taking $\tilde{\mathbf{v}} = \mathbf{v}_s$, we obtain BC1 proposed by Young *et al.* [16],

$$(\mathbf{V} - \mathbf{v}_s) \cdot \mathbf{n} = \eta \mathbf{n} \cdot [(\boldsymbol{\Sigma} - p\mathbf{I}) - (\boldsymbol{\sigma}_f - p\mathbf{I})] \cdot \mathbf{n}, \quad (15)$$

$$(\mathbf{V} - \mathbf{v}_s) \cdot \mathbf{t} = \beta \mathbf{n} \cdot \boldsymbol{\Sigma} \cdot \mathbf{t}, \quad (16)$$

$$\phi_f (\mathbf{v}_f - \mathbf{v}_s) \cdot \mathbf{t} = -\beta \mathbf{n} \cdot \boldsymbol{\sigma}_f \cdot \mathbf{t}, \quad (17)$$

where η and β are positive interfacial permeability and slip coefficients, respectively. Although the two tangential slip velocities can in principle have different slip coefficients, we use a single β for simplicity for the rest of the paper. Similarly, taking $\tilde{\mathbf{v}} = \mathbf{v}_f$ leads to BC2 of Feng and Young [17]:

$$(\mathbf{V} - \mathbf{v}_f) \cdot \mathbf{n} = \eta \mathbf{n} \cdot [(\boldsymbol{\Sigma} - p\mathbf{I}) - (\boldsymbol{\sigma}_s - p\mathbf{I})] \cdot \mathbf{n}, \quad (18)$$

$$(\mathbf{V} - \mathbf{v}_f) \cdot \mathbf{t} = \beta \mathbf{n} \cdot \boldsymbol{\Sigma} \cdot \mathbf{t}, \quad (19)$$

$$\phi_s (\mathbf{v}_s - \mathbf{v}_f) \cdot \mathbf{t} = -\beta \mathbf{n} \cdot \boldsymbol{\sigma}_s \cdot \mathbf{t}. \quad (20)$$

Finally, we take $\tilde{\mathbf{v}} = \mathbf{V}$, and derive a new set of BCs hereafter called BC3:

$$\phi_s (\mathbf{v}_s - \mathbf{V}) \cdot \mathbf{n} = \eta \mathbf{n} \cdot (\boldsymbol{\sigma}_f - \boldsymbol{\sigma}_s) \cdot \mathbf{n}, \quad (21)$$

$$\phi_f (\mathbf{v}_f - \mathbf{V}) \cdot \mathbf{t} = -\beta \mathbf{n} \cdot \boldsymbol{\sigma}_f \cdot \mathbf{t}, \quad (22)$$

$$\phi_s (\mathbf{v}_s - \mathbf{V}) \cdot \mathbf{t} = -\beta \mathbf{n} \cdot \boldsymbol{\sigma}_s \cdot \mathbf{t}. \quad (23)$$

In simplifying these, we have used the continuity and traction balance equations [Eqs. (11) and (12)]. Note that the choice of $\tilde{\mathbf{v}}$ is based on algebraic simplicity. The above three choices produce simple BCs; other choices are possible but lead to lengthier expressions. These BCs require the injection velocity to be proportional to normal stress jumps across the interface, and the slip velocities to shear stresses on either side of the interface. The latter, in particular, recalls the familiar Navier slip condition [20,21]. These observations impart certain physical meanings to the permeability and slip coefficients.

Each of the three sets of BCs has one condition for a permeation velocity and two for slip velocities. It turns out that the permeation BC is essentially the same among BC1–3. To see this, we use the fluid continuity [Eq. (11)] and overall traction balance [Eq. (12)] to transform Eqs. (15), (18), and (21) into

$$\begin{aligned} \text{BC1} : (\mathbf{V} - \mathbf{v}_s) \cdot \mathbf{n} &= \eta \mathbf{n} \cdot [(\boldsymbol{\Sigma} - p\mathbf{I}) - (\boldsymbol{\sigma}_f - p\mathbf{I})] \cdot \mathbf{n}, \\ \text{BC2} : (\mathbf{V} - \mathbf{v}_s) \cdot \mathbf{n} &= \eta \frac{\phi_f^2}{\phi_s^2} \mathbf{n} \cdot [(\boldsymbol{\Sigma} - p\mathbf{I}) - (\boldsymbol{\sigma}_f - p\mathbf{I})] \cdot \mathbf{n}, \\ \text{BC3} : (\mathbf{V} - \mathbf{v}_s) \cdot \mathbf{n} &= \eta \frac{1}{\phi_s^2} \mathbf{n} \cdot [(\boldsymbol{\Sigma} - p\mathbf{I}) - (\boldsymbol{\sigma}_f - p\mathbf{I})] \cdot \mathbf{n}. \end{aligned} \quad (24)$$

They are essentially the same in making the normal velocity jump proportional to the normal stress jump between the clear fluid outside and the pore fluid inside the gel, differing only in the coefficient. This difference is immaterial as the slip coefficient can be chosen independently for each BC. In contrast, the two slip velocities are not equivalent among the BCs. By subtracting between the two and using the overall traction balance of Eq. (12), we can obtain a third slip velocity for each BC as a linear combination of two of the three shear stresses. The consequences of the differing slip velocities among BC1–3 will be explored in two-layer shear flows (Secs. III B and III C).

In addition to the three sets of thermodynamically motivated BCs, we also include a set of BC representative of the earlier proposals. Minale [15] summarized them into two ideas: continuity of velocity across the interface, and a traction partition scheme that assigns the external traction outside the gel to the fluid and solid components inside the gel. Based on Minale's BCs, we pose the following as the fourth set of BCs to be studied below, henceforth called the BCM:

$$\mathbf{V} = \phi_f \mathbf{v}_f + \phi_s \mathbf{v}_s, \quad (25)$$

$$\mathbf{n} \cdot (\boldsymbol{\Sigma} - p\mathbf{I}) = \mathbf{n} \cdot (\boldsymbol{\sigma}_s - p\mathbf{I}) = \mathbf{n} \cdot (\boldsymbol{\sigma}_f - p\mathbf{I}). \quad (26)$$

These generalize Minale's BC in the following sense. First, Minale has no solid velocity in his rigid porous medium, and so our Eq. (25) is a generalization to deformable solid network. Note that Eq. (25) can be recast as $\mathbf{V} - \mathbf{v}_s = \phi_f (\mathbf{v}_f - \mathbf{v}_s)$. Thus, it contains the fluid continuity of Eq. (11) as its normal component, alongside a tangential component. Second, Minale expresses the traction partition in scalar form for 1D shear flow (Eq. (56) in Ref. [15]), and Eq. (26) is a more general tensorial form. Note, however, that Minale calculates the Brinkman stress using the *phase-averaged* velocity $\langle \mathbf{v} \rangle$ whereas we use the *intrinsic phase-averaged* velocity \mathbf{v}_f , with $\langle \mathbf{v} \rangle = \phi_f \mathbf{v}_f$. Thus, in connecting the two formulations, we have assumed $\nabla(\phi_f \mathbf{v}_f) = \phi_f \nabla \mathbf{v}_f$. This has been assumed by Minale [15] as well, and should be acceptable if the volume fraction varies gently in space.

C. Limiting cases

It is interesting to examine some limiting cases to understand how the proposed BCs are related to expected behavior under these conditions.

First, if the Brinkman stress is negligible ($\boldsymbol{\sigma}_f \rightarrow 0$ or $\mu_e \rightarrow 0$), we approach the Darcy limit, in which case BC1–3 turn out to be essentially the same. After omitting the $\nabla^2 \mathbf{v}_f$ term from the Brinkman equation [Eq. (6)], we no longer need the BC for \mathbf{v}_f . There are two methods for deriving the reduced BCs for a Darcy flow. One may drop the term containing $\boldsymbol{\sigma}_f$ from the interfacial

dissipation integral [Eq. (13)], and propose BCs to ensure the non-negativity of the remaining terms [17]. Alternatively, one may start with the general forms of BC1–3 and drop the BC on the slip velocity $(\mathbf{v}_f - \mathbf{v}_s) \cdot \mathbf{t}$. For BC2, one has to linearly combine two tangential velocity jump conditions to eliminate \mathbf{v}_f , and then keep the resulting condition in place of the original two. These two procedures lead to the same BCs, albeit with slightly different forms of the slip coefficient. In the notation of the second approach, the remaining BC for the tangential slip velocity becomes

$$\begin{aligned} \text{BC1} : (\mathbf{V} - \mathbf{v}_s) \cdot \mathbf{t} &= \beta \mathbf{n} \cdot \boldsymbol{\Sigma} \cdot \mathbf{t}, \\ \text{BC2} : (\mathbf{V} - \mathbf{v}_s) \cdot \mathbf{t} &= \beta \left(1 + \frac{1}{\phi_s^2} \right) \mathbf{n} \cdot \boldsymbol{\Sigma} \cdot \mathbf{t}, \\ \text{BC3} : (\mathbf{V} - \mathbf{v}_s) \cdot \mathbf{t} &= \frac{\beta}{\phi_s^2} \mathbf{n} \cdot \boldsymbol{\Sigma} \cdot \mathbf{t}, \end{aligned} \quad (27)$$

which are the same except for an inconsequential difference in the slip coefficient. As the permeation condition is essentially the same in general [Eq. (24)], BC1–3 are essentially the same in the Darcy limit. Interestingly, BCM does not have a proper Darcy limit. The traction partition of Eq. (26) cannot be implemented as the fluid phase inside the hydrogel has $\sigma_f = 0$ in Darcy flow and cannot sustain any traction.

Moreover, BCM corresponds to the limit of zero energy dissipation on the fluid-gel interface. This can be seen by substituting the velocity continuity of Eq. (25) and the traction partition of Eq. (26) into Eq. (13), and obtaining $I_\Gamma = 0$. In addition, we examine the permeation condition of BC1–3 [Eq. (24)] in the limit of $\eta \rightarrow \infty$. All three reduce to

$$\mathbf{n} \cdot [(\boldsymbol{\Sigma} - p\mathbf{I}) - (\sigma_f - p\mathbf{I})] \cdot \mathbf{n} = 0, \quad (28)$$

which, together with the total traction balance of Eq. (12), stipulates zero normal stress jump across the fluid-gel interface. This recovers the normal component of the BCM stress partition in Eq. (26) and confirms that BCM coincides with the limit of the other BCs with vanishing resistance to fluid permeation ($\eta \rightarrow \infty$). The consequences will be seen in the compression flow in Sec. III A.

For BC1 and BC2, Feng and Young [17] probed the one-phase limits of pure solid ($\phi_f \rightarrow 0$) or pure liquid ($\phi_f \rightarrow 1$) in the gel. For BC1 and BC2 to conform to expectations when the gel becomes an impermeable solid (no slip and no permeation on the interface) or a pure liquid (fluid velocity continuity), the following limiting behavior are required of the two coefficients:

- (1) Pure solid ($\phi_f \rightarrow 0$): $\beta \rightarrow 0$ and $\eta \rightarrow 0$ in BC1, $\beta \rightarrow 0$ in BC2
- (2) Pure liquid ($\phi_f \rightarrow 1$): $\beta \rightarrow 0$ in BC1, $\beta \rightarrow 0$ and $\eta \rightarrow 0$ in BC2

The new BC3 can be easily shown to be identical to BC1 in the limit of $\phi_f \rightarrow 0$, and to BC2 in the limit of $\phi_f \rightarrow 1$. We omit the derivation for brevity.

Finally, we consider the limit of a rigid solid network, in which case the gel deformation vanishes ($\mathbf{u}_s = 0, \mathbf{v}_s = 0$) and the solid stress σ_s becomes indeterminate. BC1–3 reduce to similar forms, with a normal velocity jump being proportional to a jump in normal stress at the interface, and two tangential velocity jumps being proportional to the shear stress on either side or their difference across the interface. Take BC2, for example,

$$(\mathbf{V} - \mathbf{v}_f) \cdot \mathbf{n} = -\eta \frac{\phi_f}{\phi_s} \mathbf{n} \cdot [(\boldsymbol{\Sigma} - p\mathbf{I}) - (\sigma_f - p\mathbf{I})] \cdot \mathbf{n}, \quad (29)$$

$$(\mathbf{V} - \mathbf{v}_f) \cdot \mathbf{t} = \beta \mathbf{n} \cdot \boldsymbol{\Sigma} \cdot \mathbf{t}, \quad (30)$$

$$\phi_s^2 \mathbf{v}_f \cdot \mathbf{t} = \beta \mathbf{n} \cdot (\boldsymbol{\Sigma} - \phi_f \sigma_f) \cdot \mathbf{t}. \quad (31)$$

We can identify Eq. (30) with the Beavers-Joseph condition for porous medium [6,12], where the interfacial slip velocity is proportional to the pure-fluid shear stress. Similarly, Eq. (31) can be likened to the condition of Ochoa-Tapia and Whitaker [10,15], where a slip velocity is related to the

shear stress jump across the interface. The porous-media literature typically poses an additional BC on the velocity, e.g., $\mathbf{V} = \phi_f \mathbf{v}_f$ of Minale [15], in place of our normal velocity jump.

III. RESULTS AND DISCUSSION

Feng and Young [17] concluded that to discriminate among the BCs, one needs to compute flows in complex geometries or transient conditions and with a prominent Brinkman stress. Partly for this purpose, we have recently developed a finite-element algorithm for computing fluid-hydrogel two-phase flows, using BC1 and BC2 as examples [18]. The numerical formalism can be easily adapted to BC3 and BCM (see Appendix A). In this section, we use four test problems to compare and evaluate the four BCs, BC1–3 and BCM.

The following scalings are used to render the governing equations and BCs dimensionless:

$$\begin{aligned} (\bar{x}, \bar{y}) &= (x, y)/L, \quad (\bar{\mathbf{V}}, \bar{\mathbf{v}}_s, \bar{\mathbf{v}}_f) = (\mathbf{V}, \mathbf{v}_s, \mathbf{v}_f)/V_0, \quad \bar{t} = tV_0/L, \\ \bar{\mathbf{u}}_s &= \mathbf{u}_s/L, \quad (\bar{\boldsymbol{\Sigma}}, \bar{\boldsymbol{\sigma}}_s, \bar{\boldsymbol{\sigma}}_f, \bar{P}, \bar{p}) = (\boldsymbol{\Sigma}, \boldsymbol{\sigma}_s, \boldsymbol{\sigma}_f, P, p)/\mu_s, \end{aligned} \quad (32)$$

where the overbar denotes dimensionless quantities, V_0 is the characteristic velocity, and L is the characteristic length. The dimensionless problem is then governed by the following dimensionless groups:

$$\begin{aligned} \bar{\mu}_e &= \mu_e/\mu, \quad \bar{\lambda}_s = \lambda_s/\mu_s, \quad \bar{\xi} = \xi L^2/\mu, \\ (\bar{\beta}, \bar{\eta}) &= (\beta, \eta)\mu/L, \quad \text{Ca} = V_0\mu/(L\mu_s), \quad \phi_{s0}, \end{aligned} \quad (33)$$

where ϕ_{s0} is the initial solid fraction in the undeformed hydrogel. Ca indicates the ratio between the external viscous stress and the elastic stress of the solid skeleton, and can be viewed as an effective capillary number. The following discussion will involve dimensionless quantities only and we will omit the overbar.

Based on realistic material parameters, e.g., the porosity, permeability, and moduli of hydrogels, we have estimated the dimensionless parameters of Eqs. (33). These values will be used and sometimes varied in the numerical simulations below. Not all parameters are equally important in a given problem. For example, λ_s and Ca affect the amount of solid deformation and are thus unimportant insofar as we only consider moderate deformations. The solid fraction ϕ_{s0} turns out to have only mild effects on the flow field inside the gel. Depending on whether the external flow is parallel or perpendicular to the gel interface, one of β and η may be irrelevant. Therefore, instead of a comprehensive parametric study, we will only vary the parameters most important to each flow problem.

A. One-dimensional compression

A layer of hydrogel of thickness $L = 1$ is compressed by a uniform flow along the x axis of velocity $V_0 = 1$ (Fig. 2). The hydrogel is constrained on its right surface ($x = 2L$) by a permeable plate so as to have zero displacement there. A stress-free condition for the fluid phase is also implemented at $x = 2L$. There is no flow or variation in the y direction and the problem is one-dimensional (1D). For brevity, we will omit the subscript x for the x components. Thus, the tangential or slip velocities vanish, and we need only consider BCs regarding the normal flow, i.e., permeation into the gel. As noted in Sec. IIB, these are essentially the same among BC1–3. Therefore, we will use BC1 as a representative in the rest of this subsection.

BC1 and BCM exhibit some stark differences in their steady-state pressure and velocity profiles (Fig. 3). BC1 incurs a large pressure drop across the interface [Fig. 3(a)], consistent with the intuition of a fluid flowing from free space into small pores. This can also be understood from Eq. (15), which in this geometry relates the pressure drop linearly with the free-stream velocity V_0 . In contrast, BCM predicts a slight pressure *rise* across the interface, from 0.1037 to 0.1102. This is because BCM equates the fluid normal stress on either side of the interface, and the Brinkman

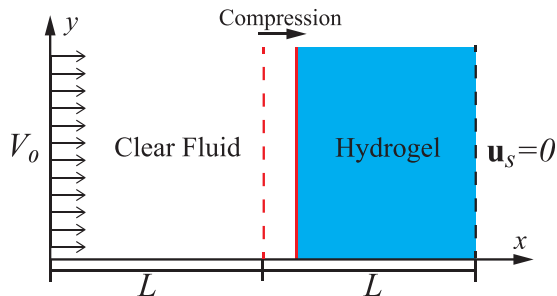


FIG. 2. A diagram showing the 1D compression of a layer of hydrogel. The dashed red line denotes the initial interface between the clear fluid and the hydrogel, and the solid red line the displaced interface under compression. The length of the computational domain is $2L$, the initial thickness of the hydrogel layer being $L = 1$. The uniform velocity of the clear fluid is $V_0 = 1$. The right surface of the gel layer is constrained by a fixed permeable plate (the black dash line) and has zero displacement.

normal stress inside the gel is tensile: $\sigma_f = 2\mu_e(dv_f/dx) > 0$ [Fig. 3(b)]. The larger pressure drop for BC1, along with the Darcy drag, causes a larger compression of the hydrogel and a larger solid stress in reaction, as is evident from the vertical dashed lines indicating the displaced interfaces. The

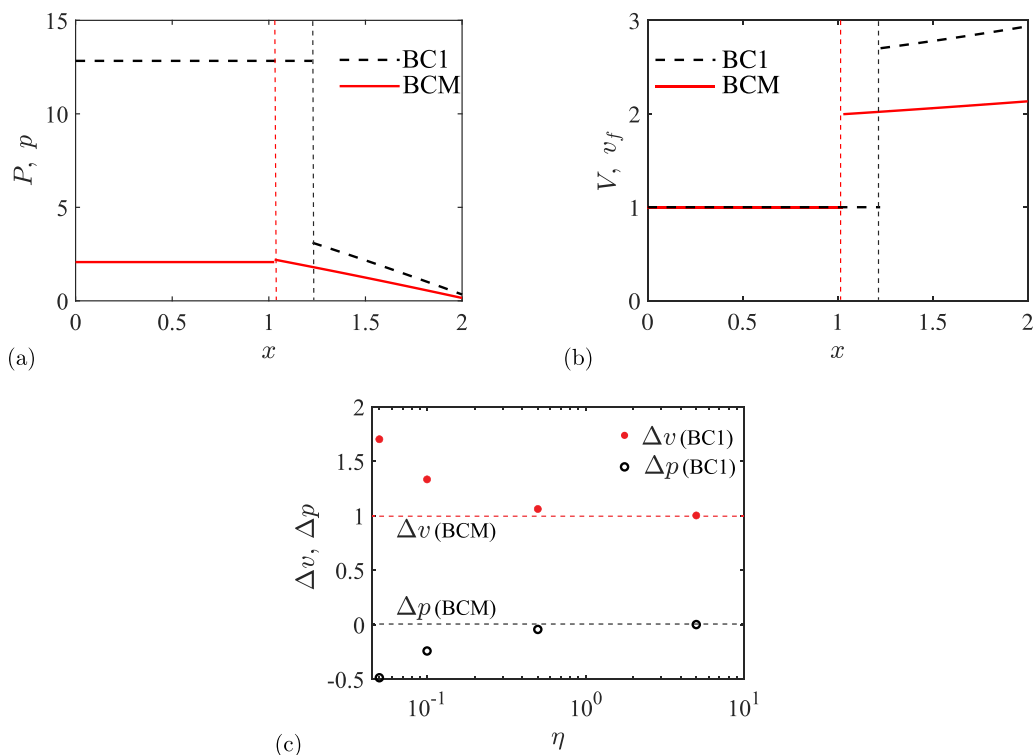


FIG. 3. Comparison between BC1 and BCM in 1D steady-state compression. (a) Pressure profiles and (b) fluid velocity profiles along the x axis. The vertical dash lines represent the location of the upstream interface (at $x = 1$ before deformation) and show greater gel compression for BC1. The parameters are $\lambda_s = 1$, $\mu_e = 1$, $\xi = 4$, $\text{Ca} = 0.025$, $\phi_{s0} = 0.5$ and for BC1, $\eta = 0.05$. (c) Interfacial jumps in pressure and velocity as functions of η .

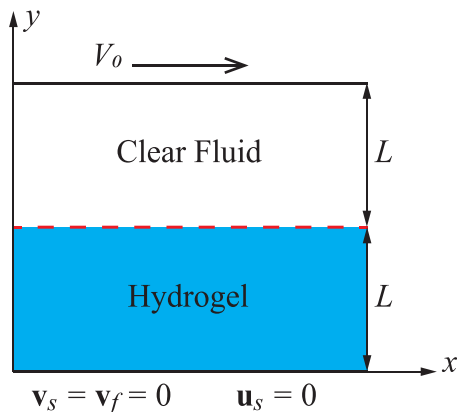


FIG. 4. The setup for a two-layer Couette flow with a layer of clear fluid atop a hydrogel layer. The lid moves with velocity $V_0 = 1$ while the bottom is fixed.

larger compression reduces ϕ_f for BC1, which in turn leads to a larger velocity jump at the interface and faster v_f inside the hydrogel [Fig. 3(b)]. For BCM, in contrast, the gel at the interface is not compressed but *stretched* slightly, from the initial $\phi_f = 0.5$ to 0.501. The solid normal stress being tensile can be inferred from BCM's traction partition scheme [Eq. (26)]: $\sigma_s = \sigma_f > 0$. Of course, the interior of the gel is compressed by the Darcy drag for BCM, resulting in the small interfacial displacement in Fig. 3(b).

The pressure and velocity jumps at the upstream interface, $\Delta p = p - P$ and $\Delta v = v_f - V$, are plotted as functions of the permeability coefficient η in Fig. 3(c). BCM does not involve η , and its Δp and Δv are represented by two horizontal dashed lines. For BC1, increasing η implies decreasing interfacial resistance to the entry of the fluid. Thus, both Δp and Δv decrease in magnitude, approaching their respective BCM levels for large η . This confirms the observation that BCM represents the large-permeability limit. With BC1, the solid compression also decreases with increasing η (results not shown).

To summarize the 1D compression test, we see similar results for BC1–3, but BCM predicts a slight pressure rise instead of a pressure drop across the fluid-gel interface and a slight expansion of the gel at the interface. These counterintuitive results can be attributed to its underlying assumption of zero resistance to fluid permeation into the hydrogel. The 1D compression test, therefore, favors BC1–3 over BCM.

B. Two-layer shear: Couette flow

Our second test, the two-layer Couette flow of Fig. 4, focuses on the tangential velocity jumps, or slip velocities, across the fluid-gel interface. A layer of clear fluid lies atop a layer of hydrogel and the thickness of both layers is unity: $L = 1$. The shear flow is driven by the lid moving with a constant velocity $V_0 = 1$. The bottom of the hydrogel is fixed where the fluid velocity and solid displacement both vanish. The initial volume fraction $\phi_{s,0} = 0.5$. The solid network inside the gel being linearly elastic, its displacement will be 1D simple shear with no vertical displacement. Thus, $\phi_f = \phi_s = 0.5$ holds at all times, and the flow and deformation will be 1D along the x direction. Another consequence of the one-dimensionality is zero fluid permeation into the gel. Thus, we need only concern ourselves with the slip coefficient β here. The slip velocities of BC1 [Eqs. (16) and (17)], BC2 [Eqs. (19) and (20)], BC3 [Eqs. (22) and (23)], and BCM [Eqs. (25) and (26)] can all be simplified into 1D forms. It turns out that the 1D steady shear flow can be solved analytically for all the BCs; see Appendix B for details.

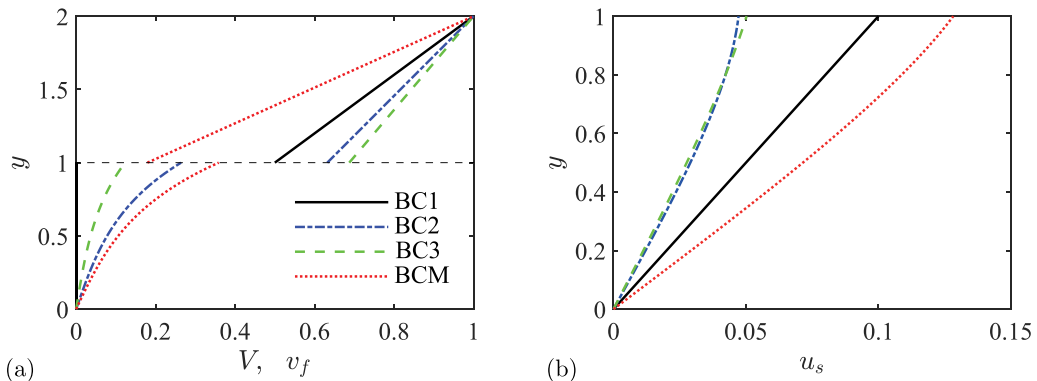


FIG. 5. Two-layer Couette flow: (a) Steady-state profiles of velocity V and v_f for the four BCs and (b) steady-state profiles of the solid displacement u_s . The dimensionless parameters are $\mu_e = 1$, $\xi = 10$, $\beta = 1$, $Ca = 0.1$, and $\phi_{s0} = 0.5$. The second Lamé constant λ_s does not appear in the simple shear.

Figure 5(a) compares the velocity profiles $V(y)$ and $v_f(y)$ of a typical steady-state Couette flow predicted by the four BCs. As noted before [17], with BC1 no flow can be generated inside the hydrogel. This is because BC1 relates the slip velocity $V - v_s$ outside the gel to the shear stress of the clear fluid outside [Eq. (16)], and the slip velocity $v_f - v_s$ inside the gel to the Brinkman stress inside [Eq. (17)]. Thus, the external and internal flows are effectively decoupled and no viscous stress from the clear fluid can be transmitted to the fluid phase of the hydrogel. The profiles for BC2 and BC3 are similar, although BC3 predicts a larger velocity jump $V - v_f$ across the interface for the current parameter set. Numerical experimentation shows that reducing the slip coefficient β tends to suppress the flow and Brinkman stress inside the gel. Then BC2 can produce a larger velocity jump than BC3 [cf. Eqs. (19) and (22)].

BCM stands out for predicting a negative velocity jump $V - v_f < 0$ across the interface due to the BC $V = \phi_f v_f$ [Eq. (25)]. Recall that v_f is the intrinsic phase-averaged velocity, i.e., the velocity of the pore fluid averaged over fluid elements alone, without the solids. As the pore fluid is hindered by the solids whereas the external fluid is not, the prediction of $v_f > V$ by BCM appears counterintuitive. We will discuss experimental evidence related to this point in Sec. III C.

Figure 5(b) depicts the displacement profiles $u_s(y)$ for the four BCs. They are qualitatively the same, and all predict the solid to slide to the right ($u_s > 0$) in the direction of the external flow. The relative magnitude of u_s can be understood from the external shear stress Σ . First, the magnitude of u_s corresponds roughly with the solid shear stress τ_s , which in turn appears to correlate with Σ or the external velocity gradient dV/dy of Fig. 5(a). Thus, BCM predicts the largest u_s because of the largest dV/dy at the interface, and BC1 has the second largest. The exact relationship between Σ and σ_s varies; BCM assumes $\Sigma = \sigma_s$ [Eq. (26)], while BC1 has $\Sigma = \phi_s \sigma_s$ with the pore fluid at rest [Eq. (12)]. With BC2 and BC3, the shear stresses Σ , σ_f and σ_s are all smaller [see velocity gradients in Fig. 5(a)], and so is their solid displacement u_s .

Among the parameters, we have explored the effects of ϕ_{s0} , ξ , and β . They turn out to have mostly quantitative effects that can be anticipated from intuition. For example, reducing the solid fraction ϕ_{s0} increases v_f in the gel but decreases the velocity jump $V - v_f$ for all BCs. Increasing the Darcy drag coefficient ξ or the slip coefficient β tends to increase $V - v_f$, the former owing to the greater hinderance to v_f and the latter directly to the BCs such as Eq. (19). Thus, we will not present these results.

We have further studied an oscillatory Couette flow by imposing a time-dependent velocity on the lid: $V_{os}(t) = V_0 \sin(\omega t)$. Although one expects the pore fluid velocity v_f and solid velocity v_s to vary periodically, the different BCs reveal different phase behaviors (Fig. 6). For BC1, the oscillatory flow in the clear fluid does drive a Brinkman flow inside the gel; this is because the solid velocity

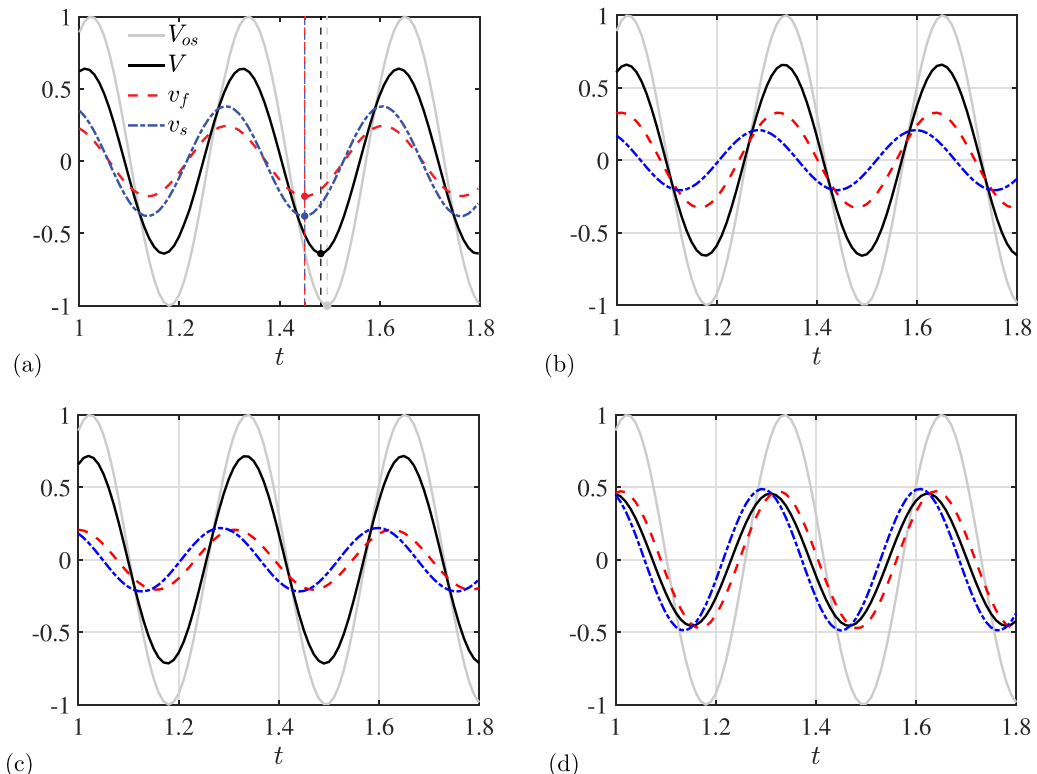


FIG. 6. Temporal evolution of the interfacial velocities V , v_f , and v_s in oscillatory Couette flow with different BCs: (a) BC1 (the vertical dashed lines mark the troughs of each curve and illustrate the phase difference among them), (b) BC2, (c) BC3, and (d) BCM. The lid velocity $V_{os}(t) = V_0 \sin(\omega t)$, with dimensionless angular frequency, scaled by the characteristic time L/V_0 , $\omega = 5$. The other parameters are the same as in the steady Couette flow.

$v_s \neq 0$ serves to connect the external and interstitial flows. Note that v_f and v_s are phase locked, and both lag the external V somewhat [Fig. 6(a)]. This can be rationalized by the BC of Eq. (17): $\phi_f(v_f - v_s) = -\beta\sigma_f$, which relates the interphasic slip velocity to the pore-fluid shear stress at the interface. As σ_f stays in phase with v_f , so does v_s . In contrast, both BC2 and BC3 show that v_s lags behind v_f [Figs. 6(b) and 6(c)]. This is because both BCs relate the velocity difference to the solid stress σ_s [Eqs. (20), (22), and (23)], which is in phase with the solid *strain* but out of phase with the solid velocity v_s . This phase lag, therefore, is a manifestation of the viscoelastic response of the gel. BCM similarly shows a phase lag of v_s behind v_f , thanks to the involvement of both the solid and fluid shear stresses in the traction partition scheme [Eq. (26)]. Because BCM directly constrains the three velocities V , v_f and v_s at the interface [Eq. (25)], V equals the average of v_f and v_s for $\phi_f = \phi_s = 0.5$, and the magnitudes of the three interfacial velocities are close at all times. Thus, the oscillatory shear test distinguishes BC1 from the other BCs for its lack of a phase lag. This is another shortcoming of BC1 that can potentially be verified by unsteady-shear experiments.

C. Two-layer shear: Poiseuille flow

Now we drive the two-layer shear flow by a constant pressure gradient $dp/dx = p_x < 0$ over the entire flow domain, including the clear fluid layer and the gel layer. Taking the characteristic velocity to be $V_0 = |p_x|L^2/\mu$, we define a capillary number Ca as before to represent the magnitude of the flow. Figure 7(a) compares the velocity profiles predicted by the various BCs for a representative

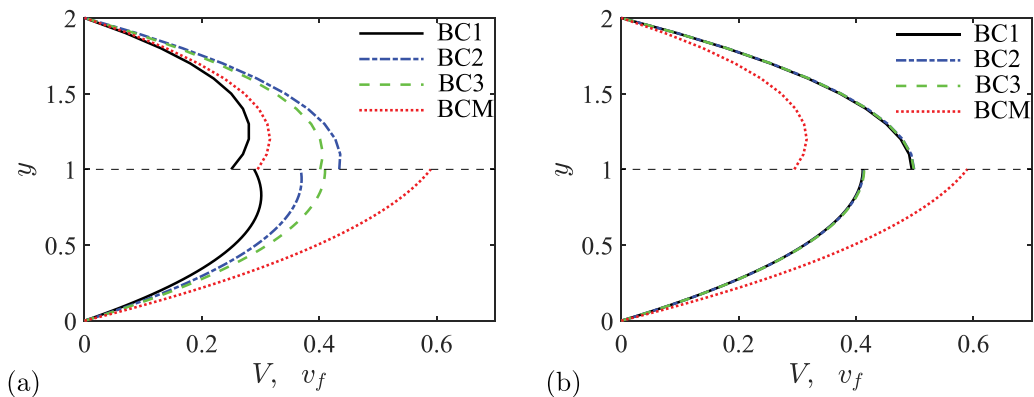


FIG. 7. Steady velocity profiles in the two-layer Poiseuille flow. (a) $V(y)$ and $v_f(y)$ for the four BCs at $\beta = 1$. (b) $V(y)$ and $v_f(y)$ for the four BCs at $\beta = 100$. The other dimensionless parameters are $\mu_e = 1$, $\xi = 1$, $\text{Ca} = 1$, and $\phi_{s0} = 0.5$.

parameter set. The velocity in the clear fluid shows the characteristic parabolic shape, while that in the gel is composed of exponential forms (see details in Appendix B). The most interesting feature is the sign of the velocity jump $V - v_f$ across the interface. BC2 stands out in predicting $V > v_f$, while BC1, BC3, and BCM all predict $V < v_f$. Since the same pressure gradient drives the flow in both layers, and inside the gel the flow is hindered by the solid skeleton, $V < v_f$ appears implausible.

As BCM enforces $V = \phi_f v_f$ [Eq. (25)], its prediction of $V < v_f$ reaffirms the same flaw as noted in the Couette flow. For BC1–3, the tangential velocity jumps can be rewritten from the respective BCs [Eqs. (16)–(22)]:

$$\begin{aligned}
 \text{BC1} : V - v_f &= \beta \left(\Sigma + \frac{\sigma_f}{\phi_f} \right), \\
 \text{BC2} : V - v_f &= \beta \Sigma, \\
 \text{BC3} : V - v_f &= \beta \frac{\sigma_f}{\phi_f},
 \end{aligned} \tag{34}$$

where Σ and σ_f are the shear stresses of the clear fluid and the interstitial fluid at the interface. As $\Sigma > 0$ is guaranteed by the Poiseuille flow in the clear fluid, BC2 always predicts $V > v_f$. For BC1 and BC3, the sign of the velocity jump depends on the Brinkman shear stress. In the solutions of Fig. 7(a), σ_f is sufficiently negative to yield the unphysical $V < v_f$. This outcome is parameter dependent, however. By increasing the Darcy drag coefficient ξ , for example, the flow inside the gel can be suppressed to reduce the magnitude of a negative σ_f for BC1 or yield a monotonic $v_f(y)$ profile with $\sigma_f > 0$ for BC3, thereby resulting in $V > v_f$. In addition, a large β would produce an essentially freely slipping interface on which both Σ and σ_f vanish. In this case, the velocity profiles for BC1–3 approach the same limit with $V > v_f$ [Fig. 7(b)]. Appendix B further discusses the parametric effects on the velocity jump and plots $V - v_f$ as a function of ξ and β in Fig. 13.

Several experiments have attempted to measure the steady-state velocity profiles in shear flows over rigid porous media [13,22–24]. But determining the velocity jump $V - v_f$ turns out to be challenging. A conceptual difficulty is the separation of length scales required by a continuum theory: the volume averaging should use a length scale much greater than the pore size and simultaneously much smaller than the macroscopic length scale of interest. Such separation becomes difficult in defining and measuring the average fluid velocity near the interface [10]. If one uses the same box size for such averaging at the interface as in the bulk, it would enclose more of the clear fluid nearer the interface. Thus, one naturally obtains a continuous profile for the average fluid velocity [13,23],

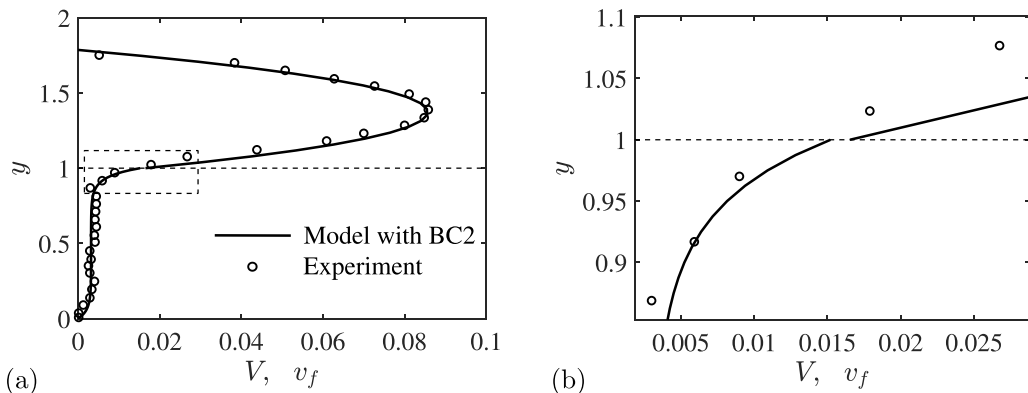


FIG. 8. (a) Comparison of measured velocity profiles in a two-layer Poiseuille flow with model predictions by BC2. The experimental data are from Fig. 7(b) of Arthur *et al.* [24] for a solid volume fraction $\phi_s = 0.22$. In our model, the only fitting parameter is the slip coefficient $\beta = 3.57 \times 10^{-3}$, chosen to match the flow in the porous medium. Their clear-fluid velocity corresponds to our $\text{Ca} = 1$ and their permeability in the porous medium to our $\xi = 1424$. The other model parameters are $\mu_e = 1$, and $\phi_s = 0.22$. (b) Magnified view of the interfacial velocity jump for the region marked by the rectangular box in (a).

which may explain the popularity of Eq. (25) of the BCM [7,10,15]. In addition, a technical challenge is to access flow fields in small pore spaces in often opaque porous mediums [13,22–24]. In possibly the most successful attempt so far, Arthur *et al.* [24] matched the refractive index between solid obstacles and the fluid to achieve optical transparency for particle image velocimetry, and constructed a highly regular porous medium made of parallel solid cylinders arranged on a regular lattice. The macroscopic lengths, the periodicity of the flow field and the geometric regularity allowed a line-averaging scheme that bypassed the issue of separation of length scales. Thus, they managed to measure the averaged velocity $\langle v \rangle$ inside the porous medium as well as the velocity V of the clear fluid outside. After converting their average fluid velocity $\langle v \rangle$ into an interstitial velocity $v_f = \langle v \rangle / (1 - \phi_s)$, we compare a representative data set with our model prediction with BC2 in Fig. 8.

Note first the relatively small magnitude of v_f in the gel [Fig. 8(a)], owing to the low permeability in the experimental porous medium. This also requires a small slip coefficient β in our model. Under these conditions, BC2 predicts a small velocity jump $V - v_f > 0$, more easily visible in the magnified view of Fig. 8(b). If we extrapolate the nearby data points toward the interface, the experimental data also show a positive velocity jump $V - v_f$ of comparable magnitude, thus casting doubt on the velocity continuity of BCM. Finally, with one fitting parameter β , the model captures the experimental profiles remarkably well, including the transition layer just inside the porous medium that has been a focus of past studies [6,11,13,23].

To summarize the findings in 1D Couette and Poiseuille flows, BC1 effectively decouples the clear fluid from the pore fluid in steady shear flows. In steady Couette flows, BC1 predicts no flow inside the gel at all. BCM may be faulted for its implication of zero interfacial dissipation. It predicts a velocity jump across the interface that is opposite in sign to BC2 and BC3. In oscillatory Couette shear, BC2, BC3 and BCM all predict a phase lag of the solid velocity relative to the fluid velocity in the gel, whereas BC1 does not. In steady Poiseuille flow, BC2 always predicts the correct sign for the interfacial velocity jump ($V - v_f > 0$), supported by available experimental evidence, whereas BCM always the wrong sign. BC1 and BC3 can produce either sign depending on the values of the Darcy drag coefficient ξ and the interfacial slip coefficient β . Thus, our shear flow tests favor BC2, and reveal clear flaws in BC1 and BCM.

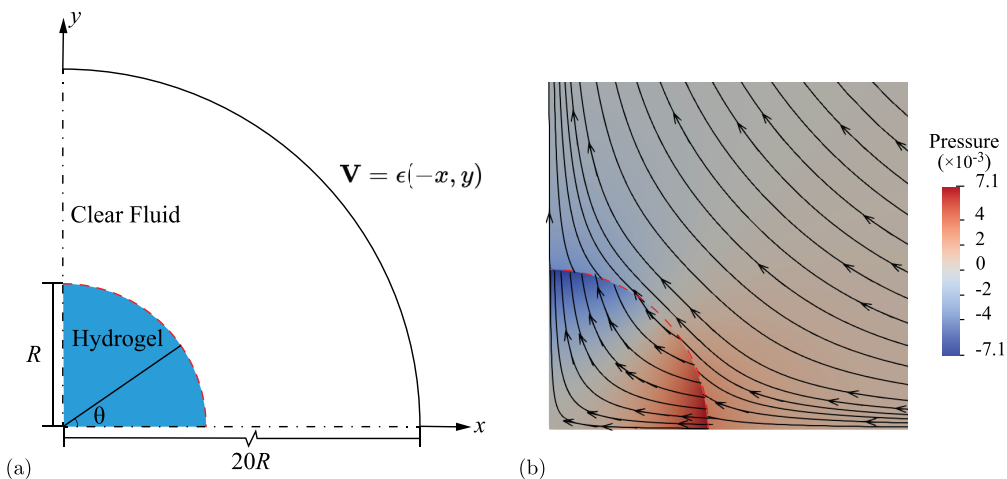


FIG. 9. (a) Computational domain for a hydrogel particle being deformed by a planar extensional flow. The polar angle θ is measured from the x axis, with the hydrogel subject to compression at $\theta = 0^\circ$, predominantly shear at $\theta = 45^\circ$ and stretching at $\theta = 90^\circ$. (b) Streamlines and pressure contours in a steady flow with BC2, at $\mu_e = 1$, $\lambda_s = 1$, $\xi = 10$, $\text{Ca} = 0.0025$, $\phi_{s0} = 0.5$, $\beta = 0.2$ and $\eta = 1$. The red dashed line marks the initial position of the interface, but the amount of deformation is minute. The apparent discontinuity in the streamlines is due to the velocity jump across the interface.

D. Deformation of a hydrogel particle in extensional flow

For its more complex 2D geometry, the final test problem requires a numerical solution, with the computational domain depicted in Fig. 9(a). More details of the finite-element formulation and numerical validation can be found in Li *et al.* [18]. A hydrogel particle with a circular undeformed shape is placed at the center of a planar extensional flow. Thanks to symmetry, we only compute the first quadrant of the flow. We choose the radius of the particle R as the characteristic length and $V_0 = \epsilon R$ as the characteristic velocity, ϵ being the extensional rate of the undisturbed flow. The outer boundary is an arc of radius $20R$, on which the undisturbed flow field $\mathbf{V} = \epsilon(-x, y)$ is imposed. Numerical tests show the domain to be large enough for the results to be independent of the domain size. On the left and bottom boundaries, symmetry conditions prevail. The hydrogel particle is squeezed horizontally and stretched vertically by the external flow.

Recall that in the limit of Darcy flow, BC1–3 are essentially the same (Sec. II C). Now we investigate how BC1–3 and BCM may produce different results in Brinkman flows. We use a low $\text{Ca} = 0.0025$ to maintain small deformation of the hydrogel particle, such that ϕ_s does not deviate much from the initial volume fraction $\phi_{s0} = 0.5$. Thus, if we choose the slip and permeability coefficients to match BC1–3 based on ϕ_{s0} , the three BCs should produce approximately the same Darcy solutions. More specifically, we use Eqs. (24) and (27) to set $\eta_{\text{BC1}} = \eta_{\text{BC2}} = 4\eta_{\text{BC3}} = 1$ and $\beta_{\text{BC1}} = 5\beta_{\text{BC2}} = 4\beta_{\text{BC3}} = 1$. Then BC1–3 are the same for Darcy flow based on the undeformed ϕ_{s0} . This common baseline facilitates the comparison below. The Brinkman solutions can still differ, of course. We have also explored large-deformation solutions, with strains up to 10%. The results are qualitatively the same and confirm our observations below of the differences among the BCs.

The flow around the gel particle is 2D and more complex than the other test problems. Figure 9(b) depicts the flow and pressure field around the gel particle in steady state. The solid deformation changes from predominantly compression at the upstream stagnation point on the particle ($\theta = 0^\circ$) to predominantly shear at the 45° point, and finally to stretching at the downstream stagnation point ($\theta = 90^\circ$). In what follows, we will focus on the solution in the two regions around $\theta = 0^\circ$ and 45° . For the relatively small deformations involved, the stretching at $\theta = 90^\circ$ is roughly a mirror image of the compression at $\theta = 0^\circ$, and offers no new insight.

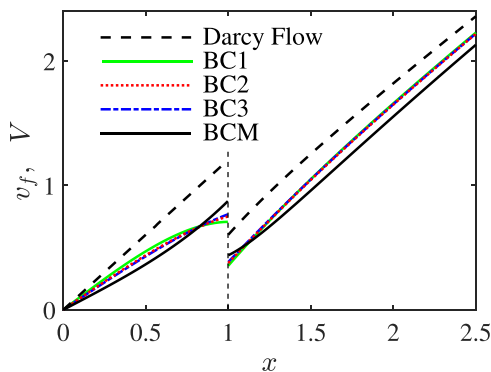


FIG. 10. Comparison of the predictions of BC1–3 and BCM: The fluid velocity profiles $v_f(x)$ and $V(x)$ along the incoming streamline ($\theta = 0^\circ$). The dimensionless parameters are $\mu_e = 1$, $\lambda_s = 1$, $\xi = 10$, $\text{Ca} = 0.0025$, and $\phi_{s0} = 0.5$. The interfacial slip and permeability coefficients are matched among BC1–3 in the Darcy limit: $\eta_{\text{BC1}} = \eta_{\text{BC2}} = 4\eta_{\text{BC3}} = 1$, $\beta_{\text{BC1}} = 5\beta_{\text{BC2}} = 4\beta_{\text{BC3}} = 1$. The Darcy solution is also shown for comparison. The interfacial compression is on the order of $u_s \sim -0.006$ for all BCs, and hardly visible in the plot.

Figure 10 compares the horizontal velocity profiles $v_f(x)$ and $V(x)$ along the x axis. We observe essentially the same trends as in the 1D compression test of Sec. III A. For instance, BC1–3 predict essentially the same solution. There are small differences in the v_f profiles, especially for BC1. This is because the permeability parameter is matched for the Darcy flow using the undeformed ϕ_{s0} , whereas we are showing results of Brinkman flow, with small solid deformation. Besides, BCM predicts smaller compression of the gel than the other three BCs, although the interfacial displacement is too small to be visible in Fig. 10. As noted before, this is because BCM allows free permeation. Unlike in 1D compression, here BCM predicts a slightly larger interstitial velocity v_f than the other BCs. As the fluid can go around the gel particle in the 2D geometry here, the greater compression for BC1–3 yields a smaller v_f . Finally, for all BCs the velocity v_f is reduced from that of the Darcy flow by the fluid viscosity inside the gel. The velocity outside V is also reduced as required by fluid continuity [Eq. (11)].

The flow in the shear-dominated region along the $\theta = 45^\circ$ radius, depicted in Fig. 11, largely mirrors the features observed in the 1D shear flows. BCM is distinct from BC1–3 in predicting a negative slip velocity: $V - v_f < 0$. This has been analyzed in the 1D Couette and Poiseuille tests,

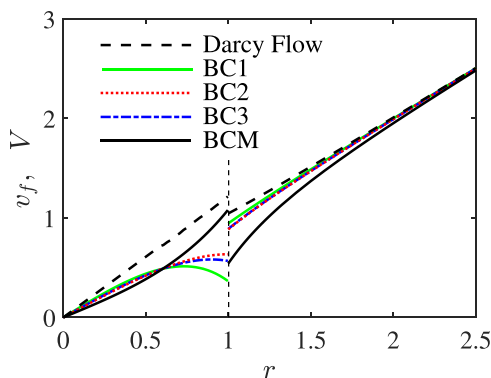


FIG. 11. Comparison of the predictions of BC1–3 and BCM: The tangential velocity profiles $v_f(r)$ and $V(r)$ along the radius $\theta = 45^\circ$ for the same solutions as depicted in Fig. 10.

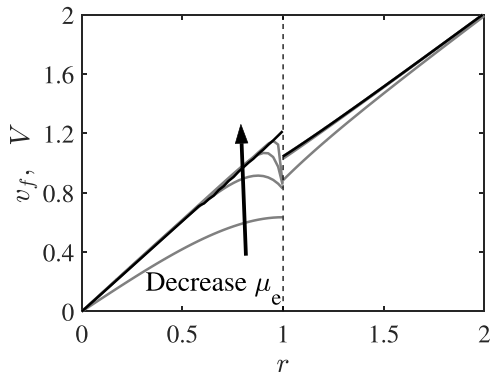


FIG. 12. The tangential velocity profile along the $\theta = 45^\circ$ radius shows a boundary layer inside the gel surface as the effective viscosity μ_e decreases: $\mu_e = 1, 0.1, 0.01, 0.001$ (grey lines; black arrow indicates decreasing μ_e). The black profile is the Darcy limit ($\mu_e = 0$). This feature is common to BC1–3 and the BC2 solution is shown here for illustration. The other parameters are the same as in Fig. 10.

and requires no more discussion here. The velocity profiles $v_f(r)$ for BC1, BC2, and BC3 are similar, all exhibiting a curvature reminiscent of that in the Poiseuille flow of Fig. 7(a). This is perhaps to be expected, as the fluid injected into the gel along the x axis flows under a pressure gradient in the interior of the gel particle. The curvature is most pronounced for BC1, as its tangential slip velocity is directly related to the local Brinkman shear stress [Eq. (17)]: $v_f = -(\beta/\phi_f)\sigma_f$. Thus, for v_f to be positive, σ_f must be negative at the interface. This, in turn, requires the nonmonotonic shape for the $v_f(r)$ profile.

In summary, the 2D flow around the gel particle largely confirms observations from 1D compression and shear flows. Although this 2D test adds little to our assessment of the BCs, it suggests that the conclusions drawn from the 1D tests will likely carry over to multidimensional flow problems.

We end this section by pointing out an interesting common feature of the solutions predicted by BC1–3: a boundary layer in the Brinkman velocity profile near the gel surface. Using BC2 for illustration, Fig. 12 shows that with decreasing effective viscosity μ_e for the interstitial fluid, the bulk velocity v_f increases toward the Darcy limit, while on the interface v_f is pinned down by the BC. The resulting boundary layer on the gel side of the interface reflects the fact that a small μ_e in the Brinkman solution represents a singular perturbation of the Darcy solution. This scenario is analogous to the classical boundary layer that bridges an exterior inviscid flow to a solid boundary at which the velocity must vanish.

IV. CONCLUDING REMARKS

A mixture theory offers the convenience of ignoring the geometric details on the pore scale, at the price of requiring additional constitutive equations governing the transport across phase boundaries. In the fluid dynamics of hydrogels, these new requirements amount to additional BCs at the interface between a hydrogel and a clear fluid, the latter being the same fluid as permeates the gel. Specifically, such BCs may describe the normal and tangential velocity jumps across the interface, i.e., differences among these three velocities: \mathbf{V} for the external fluid, \mathbf{v}_f for the interstitial fluid in the gel, and \mathbf{v}_s for the solid network in the gel. This paper aims to test four such BCs (BC1–3 and BCM) in several flow scenarios: 1D compression, 1D shear driven by a sliding lid (Couette flow) or a constant pressure gradient (Poiseuille flow), and a planar extensional flow around a gel particle. Our main findings can be summarized as follows:

(1) For 1D compression, BCM stands out as potentially flawed for its counterintuitive predictions, including a pressure rise as the fluid enters the gel and a local expansion of the gel at the interface. The overall compression of the gel layer is also very small.

(2) For 1D Couette flows, BC1 is flawed in decoupling the flow of the interstitial fluid from that of the clear fluid. This leads to zero steady-state flow inside the gel and the lack of viscoelastic response in oscillatory shear. In steady Couette flow, BCM is suspicious for predicting a counterintuitive velocity jump: a higher fluid velocity inside the gel than in the clear fluid.

(3) For 1D Poiseuille flow, BC2 is the only one that guarantees a higher fluid velocity in the clear fluid than in the gel, which is expected on physical grounds and supported by experimental evidence. BCM always predicts a faster fluid flow in the gel than outside, as do BC1 and BC3 for certain parameter ranges.

(4) The 2D planar extensional flow around a gel particle largely confirms the above observations in 1D compression and shear tests, and adds little new evidence for judging the BCs. But this suggests that the conclusions drawn from the 1D tests will probably hold in multi-dimensional flow problems as well.

(5) The failings of BCM can be traced to its assuming zero energy dissipation on the fluid-hydrogel interface. The different predictions among BC1–3 are due to algebraic details in their formulation.

Based on these, we recommend BC2 for studying the fluid dynamics of a hydrogel interface with a surrounding fluid. A finite-element algorithm for computing fluid-hydrogel two-phase flows has recently appeared [18].

For testing the BCs, we have used simple flow geometries in the above and made additional simplifying assumptions. First, we have used a linearly elastic constitutive equation for the solid network, which holds in the limit of small strains. For more complex flows with large strains, hyperelastic models should be used, such as the Saint Venant–Kirchhoff model used by Li *et al.* [18]. Then the solutions may show novel nonlinear features. For example, the simple shear of Sec. III B will incur normal stress effects and transverse deformation of the gel layer. Such features may provide additional tests for the BCs. Moreover, we have assumed the fluid-gel interface to be without surface tension or surface rheology. In reality, such interfacial effects may be important factors [25,26].

This paper has evaluated the different behaviors of the BCs by analytical and numerical solutions. It will be desirable to test them by experiments as well. Such experiments will serve as the ultimate test for the various BCs and our theoretically based recommendation. There have been efforts to measure the velocity profiles in steady two-layer shear flows over a rigid porous medium, especially pressure-driven Poiseuille flows [13,22–24]. But most have encountered difficulties in defining a properly averaged velocity near the interface and in accessing pore-scale flow fields. The most reliable data so far [24] suggests a positive velocity jump $V - v_f > 0$, with faster flow on the clear-fluid side of the interface than on the porous side, in support of the predictions by BC2. But more evidence needs to be collected in future experiments with higher spatial resolutions, especially in stochastic geometries and microscopic length scales pertinent to hydrogels. In addition to steady shear, oscillatory shear experiments similar to that of Hobbie *et al.* [27] may shed light on the phase lag between the fluid and solid deformations inside the gel. Compression experiments may clarify the correlation between solid strain and fluid flow.

Interfacial instability may provide another class of flows for testing fluid-gel interfacial BCs. There is a rich literature on elastohydrodynamic instability of compliant solid walls under the impact of flow [28–30]. More recently, linear instability over a poroelastic wall has been examined [31]. By making the permeability and slip coefficients vary with the porosity ϕ_f , the BCs considered here can be extended to the limit of impermeable walls as $\phi_f \rightarrow 0$ [17]. Thus, one can use the BCs to study interfacial instability with impermeable and permeable walls, and the results may shed new light on the suitability of the BCs.

ACKNOWLEDGMENTS

J.J.F. acknowledges the financial support by Natural Sciences and Engineering Research Council of Canada (Discovery Grant No. 2019-04162). P.Y. acknowledges the financial support by National Science Foundation (Grant No. DMS-2012480). Y.-N.Y. acknowledges support from the National Science Foundation (Grants No. DMS 1614863 and No. DMS 195160) and Flatiron Institute, part of Simons Foundation. J.Z. was partially supported by the National Science Foundation (Grants No. OAC-2015848 and No. EAR-1925575) and the Computational Infrastructure in Geodynamics initiative (through the National Science Foundation EAR-1550901 and the University of California-Davis). We thank Mattia Bacca for helpful discussions.

APPENDIX A: FINITE-ELEMENT FORMULATION

In recent work [18], we developed a finite-element algorithm to solve the coupled motion and deformation of a fluid-hydrogel system, using BC1 and BC2 as BCs. The code is based on an open-source finite-element library deal.II [32]. In the following, we briefly summarize the weak-form formalism, with special attention to BC3 and BCM as these were not considered in the earlier publication.

To obtain a weak solution of \mathbf{V} , P , \mathbf{v}_f , \mathbf{v}_s , \mathbf{u}_s , p , and ϕ_s , we define the corresponding test functions $\Psi_{\mathbf{V}}$, Ψ_P , $\Psi_{\mathbf{v}_f}$, $\Psi_{\mathbf{v}_s}$, $\Psi_{\mathbf{u}_s}$, Ψ_p , and Ψ_{ϕ_s} , respectively. The weak form of Eqs. (1), (2), and (5)–(7) can be obtained by taking the inner products of Eq. (1) with Ψ_P , Eq. (2) with $\Psi_{\mathbf{V}}$ in Ω_o , Eq. (5) with Ψ_p , Eq. (6) with $\Psi_{\mathbf{v}_f}$, and finally Eq. (7) with $\Psi_{\mathbf{v}_s}$ in Ω_i . Summing all these inner products and integrating by parts, we obtain the weak form for the governing equations:

$$\begin{aligned}
 & (\boldsymbol{\Sigma}, \nabla \Psi_{\mathbf{V}})_{\Omega_o} - ((\boldsymbol{\Sigma} - P\mathbf{I}) \cdot \mathbf{n}, \Psi_{\mathbf{V}})_{\partial\Omega_o} - (P, \nabla \cdot \Psi_{\mathbf{V}})_{\Omega_o} + (\nabla \cdot \mathbf{V}, \Psi_P)_{\Omega_o} + (\phi_f \boldsymbol{\sigma}_f, \nabla \Psi_{\mathbf{v}_f})_{\Omega_i} \\
 & - (\phi_f (\boldsymbol{\sigma}_f - p\mathbf{I}) \cdot \mathbf{n}, \Psi_{\mathbf{v}_f})_{\partial\Omega_i} + (\phi_s \boldsymbol{\sigma}_s, \nabla \Psi_{\mathbf{v}_s})_{\Omega_i} - (\phi_s (\boldsymbol{\sigma}_s - p\mathbf{I}) \cdot \mathbf{n}, \Psi_{\mathbf{v}_s})_{\partial\Omega_i} \\
 & - (p, \nabla \cdot (\phi_f \Psi_{\mathbf{v}_f} + \phi_s \Psi_{\mathbf{v}_s}))_{\Omega_i} + (\nabla \cdot (\phi_f \mathbf{v}_f + \phi_s \mathbf{v}_s), \Psi_p)_{\Omega_i} \\
 & + (\xi \phi_f \phi_s (\mathbf{v}_f - \mathbf{v}_s), \Psi_{\mathbf{v}_f} - \Psi_{\mathbf{v}_s})_{\Omega_i} = 0,
 \end{aligned} \tag{A1}$$

where (\cdot, \cdot) denotes the inner product over the region specified by the subscript. The bulk terms are straightforward, and we focus on the boundary terms. Noting that \mathbf{n} points outward of each domain in the above, we convert to a uniform notation with \mathbf{n} pointing from the gel domain to the fluid domain, and denote the fluid-gel interface by Γ . Now the three boundary terms can be collected into the following:

$$S = ((\boldsymbol{\Sigma} - P\mathbf{I}) \cdot \mathbf{n}, \Psi_{\mathbf{V}})_{\Gamma} - (\phi_f (\boldsymbol{\sigma}_f - p\mathbf{I}) \cdot \mathbf{n}, \Psi_{\mathbf{v}_f})_{\Gamma} - (\phi_s (\boldsymbol{\sigma}_s - p\mathbf{I}) \cdot \mathbf{n}, \Psi_{\mathbf{v}_s})_{\Gamma}. \tag{A2}$$

Following the same procedure as outlined by Li *et al.* [18], we obtain the weak form for BC1–3 as follows:

$$\begin{aligned}
 S_{\text{BC1}} &= \left(\frac{1}{\eta} (\mathbf{V} - \mathbf{v}_s) \cdot \mathbf{n}, (\Psi_{\mathbf{V}} - \Psi_{\mathbf{v}_s}) \cdot \mathbf{n} \right)_{\Gamma} + \left(\frac{1}{\beta} (\mathbf{V} - \mathbf{v}_s) \cdot \mathbf{t}, \Psi_{\mathbf{V}} - \Psi_{\mathbf{v}_s} \right)_{\Gamma} \\
 &+ \left(\frac{\phi_f^2}{\beta} (\mathbf{v}_f - \mathbf{v}_s) \cdot \mathbf{t}, \Psi_{\mathbf{v}_f} - \Psi_{\mathbf{v}_s} \right)_{\Gamma},
 \end{aligned} \tag{A3}$$

$$\begin{aligned}
 S_{\text{BC2}} &= \left(\frac{1}{\eta} (\mathbf{V} - \mathbf{v}_f) \cdot \mathbf{n}, (\Psi_{\mathbf{V}} - \Psi_{\mathbf{v}_f}) \cdot \mathbf{n} \right)_{\Gamma} + \left(\frac{1}{\beta} (\mathbf{V} - \mathbf{v}_f) \cdot \mathbf{t}, \Psi_{\mathbf{V}} - \Psi_{\mathbf{v}_f} \right)_{\Gamma} \\
 &+ \left(\frac{\phi_s^2}{\beta} (\mathbf{v}_s - \mathbf{v}_f) \cdot \mathbf{t}, \Psi_{\mathbf{v}_s} - \Psi_{\mathbf{v}_f} \right)_{\Gamma},
 \end{aligned} \tag{A4}$$

$$\begin{aligned}
 S_{BC3} = & \left(\frac{\phi_s^2}{\eta} (\mathbf{v}_s - \mathbf{V}) \cdot \mathbf{n}, (\Psi_{\mathbf{v}_s} - \Psi_{\mathbf{V}}) \cdot \mathbf{n} \right)_{\Gamma} + \left(\frac{\phi_s^2}{\beta} (\mathbf{v}_s - \mathbf{V}) \cdot \mathbf{t}, \Psi_{\mathbf{v}_s} - \Psi_{\mathbf{V}} \right)_{\Gamma} \\
 & + \left(\frac{\phi_f^2}{\beta} (\mathbf{v}_f - \mathbf{V}) \cdot \mathbf{t}, \Psi_{\mathbf{v}_f} - \Psi_{\mathbf{V}} \right)_{\Gamma}, \quad (\text{A5})
 \end{aligned}$$

where \mathbf{t} is the tangential vector on the interface.

BCM differs from BC1–3 in its continuous velocity [Eq. (25)] and scheme of traction partition [Eq. (26)]. First, the test function for velocity should satisfy the same constraint as Eq. (25):

$$\Psi_{\mathbf{V}}|_{\Gamma} = (\phi_f \Psi_{\mathbf{v}_f} + \phi_s \Psi_{\mathbf{v}_s})|_{\Gamma}. \quad (\text{A6})$$

Substituting $\Psi_{\mathbf{V}}|_{\Gamma}$ into Eq. (A2), we have

$$S_{BCM} = (\phi_f (\boldsymbol{\Sigma} - P\mathbf{I} - (\boldsymbol{\sigma}_f - p\mathbf{I})) \cdot \mathbf{n}, \Psi_{\mathbf{v}_f})_{\Gamma} + (\phi_s (\boldsymbol{\Sigma} - P\mathbf{I} - (\boldsymbol{\sigma}_s - p\mathbf{I})) \cdot \mathbf{n}, \Psi_{\mathbf{v}_s})_{\Gamma}. \quad (\text{A7})$$

But the stress partition of Eq. (26) ensures that $(\boldsymbol{\Sigma} - P\mathbf{I} - (\boldsymbol{\sigma}_f - p\mathbf{I})) \cdot \mathbf{n} = 0$ and $(\boldsymbol{\Sigma} - P\mathbf{I} - (\boldsymbol{\sigma}_s - p\mathbf{I})) \cdot \mathbf{n} = 0$. Therefore, the boundary terms in the weak form for BCM amount to $S_{BCM} = 0$.

APPENDIX B: ANALYTICAL SOLUTIONS OF STEADY SHEAR FLOWS

In the 1D Couette and Poiseuille flows (Sec. III B and III C), ϕ_s and ϕ_f do not deviate from their uniform initial values and can thus be treated as constants. The governing equations [Eqs. (6) and (7)] can be simplified thus:

$$\frac{d\sigma_f}{dy} - p_x - \xi \phi_s v_f = 0, \quad (\text{B1})$$

$$\frac{d\sigma_s}{dy} - p_x + \xi \phi_f v_f = 0, \quad (\text{B2})$$

with the solid stress $\sigma_s = \mu_s du_s/dy$ and fluid stress $\sigma_f = \mu_e dv_f/dy$. The Stokes equation for the clear fluid reduces to

$$\frac{d\Sigma}{dy} - p_x = 0, \quad (\text{B3})$$

in which $\Sigma = \mu dV/dy$ in dimensionless form and $p_x = dp/dx$ is the constant pressure gradient. From these equations, we obtain the general solution for the velocity profiles $V(y)$ and $v_f(y)$:

$$V(y) = \frac{p_x}{2\mu} y^2 + C_1 y + C_2, \quad (\text{B4})$$

$$v_f(y) = C_3 e^{\sqrt{\xi} \phi_s / \mu_e y} + C_4 e^{-\sqrt{\xi} \phi_s / \mu_e y} - \frac{p_x}{\xi \phi_s}. \quad (\text{B5})$$

The four-integral constant $C_{1,2,3,4}$ can be determined by the no-slip BC on the top and bottom boundaries and the interfacial BCs. The top and bottom BC can be written as

$$V(2L) = V_0, \quad v_f(0) = 0. \quad (\text{B6})$$

Along the interface $y = L$, BC1–3 and BCM can be simplified into the following:

$$\text{BC1 : } V = \beta_1 \Sigma, \quad \phi_f v_f = -\beta_2 \sigma_f, \quad (\text{B7})$$

$$\text{BC2 : } V - v_f = \beta_1 \Sigma, \quad -\phi_s v_f = -\beta_2 \sigma_s, \quad (\text{B8})$$

$$\text{BC3 : } \phi_f (v_f - V) = -\beta_1 \sigma_f, \quad -\phi_s V = -\beta_2 \sigma_s, \quad (\text{B9})$$

$$\text{BCM : } V = \phi_f v_f, \quad \Sigma = \sigma_f. \quad (\text{B10})$$

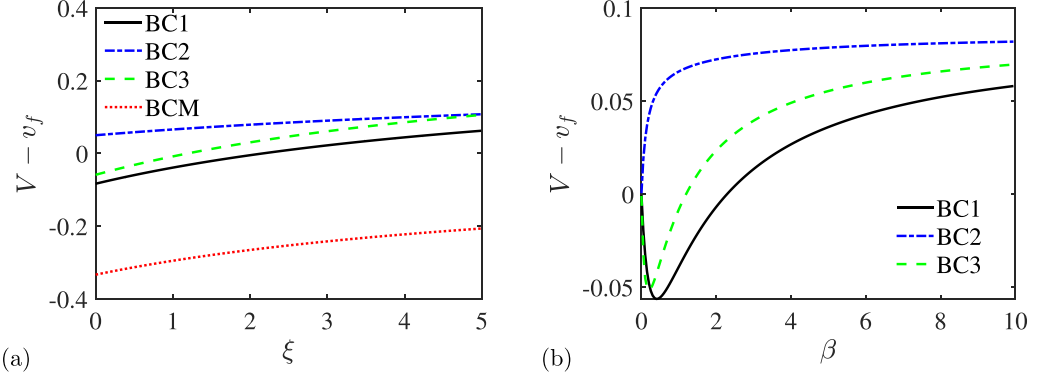


FIG. 13. Parametric dependence of the tangential velocity jump $V - v_f$ across the interface for BC1–3 and BCM in steady Poiseuille flow. (a) Variation with the Darcy drag coefficient ξ , with $\beta = 1$. (b) Variation with the permeability coefficient β , with $\xi = 1$. BCM does not have a β parameter and is thus absent. The other dimensionless parameters take the same values as in Fig. 7.

After lengthy but straightforward calculations, the velocity profiles $V(y)$ and $v_f(y)$ can be obtained. We omit the full expressions for their algebraic complexity, and focus instead on the tangential velocity jump $V - v_f$ across the interface to provide supporting details to an argument in Sec. III C.

For the 1D Poiseuille flow, we study how $V - v_f$ may change signs with the Darcy drag coefficient ξ and the interfacial permeability β for the different BCs. To simplify the algebra, we take concrete values for the dimensionless effective viscosity $\mu_e = 1$ and the solid fraction $\phi_s = 0.5$. Then the velocity jumps for the four BCs can be written as

$$\text{BC1 : } V - v_f = \frac{\beta}{2(\beta + 1)} - \frac{2\sqrt{2}\beta(\alpha - 1)^2}{\sqrt{\xi}[(\alpha^2 - 1) + \sqrt{2\xi}\beta(\alpha^2 + 1)]}, \quad (\text{B11})$$

$$\text{BC2 : } V - v_f = \frac{\beta[\xi(\alpha^2 - 1) + \sqrt{2}\beta\xi^{3/2}(\alpha^2 + 1) - 4\sqrt{2}\beta\sqrt{\xi}(\alpha - 1)^2]}{2\xi[(1 + 5\beta)(\alpha^2 - 1) + \sqrt{2\xi}\beta(\beta + 1)(\alpha^2 + 1)]}, \quad (\text{B12})$$

$$\text{BC3 : } V - v_f = \frac{2\sqrt{2}\beta[\beta\xi(\alpha^2 + 1) - (4\beta + 1)(\alpha - 1)^2]}{\sqrt{\xi}[(1 + 4\beta)(\alpha^2 - 1) + 2\sqrt{2\xi}\beta(2\beta + 1)(\alpha^2 + 1)]}, \quad (\text{B13})$$

$$\text{BCM : } V - v_f = -\frac{(\alpha - 1)(\sqrt{\xi}(\alpha + 1) + 2\sqrt{2}(\alpha - 1))}{2(\sqrt{\xi}(\alpha^2 - 1) + \sqrt{2\xi}(\alpha^2 + 1))}, \quad (\text{B14})$$

in which $\alpha = e^{\sqrt{\xi}/2}$. In Fig. 13, we compare the velocity jumps among the four BCs as functions of ξ and β . As stated in Sec. III C, only BC2 guarantees $V - v_f > 0$ for all parameter values. BC1 and BC3 can both predict $V - v_f < 0$ for smaller values of β and ξ . They also both vary nonmonotonically with β . BCM always predicts $V - v_f < 0$ according to its velocity continuity BC [Eq. (B10)].

-
- [1] E. L. Doherty, W. Y. Aw, A. J. Hickey, and W. J. Polacheck, Microfluidic and organ-on-a-chip approaches to investigate cellular and microenvironmental contributions to cardiovascular function and pathology, *Front. Bioeng. Biotechnol.* **9**, 624435 (2021).
- [2] M. Tunesi, L. Izzo, I. Raimondi, D. Albani, and C. Giordano, A miniaturized hydrogel-based in vitro model for dynamic culturing of human cells overexpressing beta-amyloid precursor protein, *J. Tissue Eng.* **11**, 2041731420945633 (2020).

- [3] R. Burrige and J. B. Keller, Poroelasticity equations derived from microstructures, *J. Acoust. Soc. Am.* **70**, 1140 (1981).
- [4] J. M. Carcione, Biot theory for porous media, in *Wave Fields in Real Media*, 3rd ed. (Elsevier, Oxford, 2015), Chap. 7, pp. 299–420.
- [5] C. W. MacMinn, E. R. Dufresne, and J. S. Wettlaufer, Large Deformations of a Soft Porous Material, *Phys. Rev. Appl.* **5**, 044020 (2016).
- [6] G. S. Beavers and D. D. Joseph, Boundary conditions at a naturally permeable wall, *J. Fluid Mech.* **30**, 197 (1967).
- [7] G. Neale and W. Nader, Practical significance of Brinkman’s extension of Darcy’s law: Coupled parallel flows within a channel and a bounding porous medium, *Can. J. Chem. Eng.* **52**, 475 (1974).
- [8] J. A. Ochoa-Tapia and S. Whitaker, Momentum transfer at the boundary between a porous medium and a homogeneous fluid. II. Comparison with experiment, *Int. J. Heat Mass Transfer* **38**, 2647 (1995).
- [9] M. Le Bars and M. G. Worster, Interfacial conditions between a pure fluid and a porous medium: Implications for binary alloy solidification, *J. Fluid Mech.* **550**, 149 (2006).
- [10] J. A. Ochoa-Tapia and S. Whitaker, Momentum transfer at the boundary between a porous medium and a homogeneous fluid.- I. Theoretical development, *Int. J. Heat Mass Transfer* **38**, 2635 (1995).
- [11] D. A. Nield and A. Bejan, *Mechanics of Fluid Flow Through a Porous Medium* (Springer, New York, 1999), Chap. 1, pp. 1–22.
- [12] B. Alazmi and K. Vafai, Analysis of fluid flow and heat transfer interfacial conditions between a porous medium and a fluid layer, *Int. J. Heat Mass Transfer* **44**, 1735 (2001).
- [13] C. Carotenuto and M. Minale, Shear flow over a porous layer: Velocity in the real proximity of the interface via rheological tests, *Phys. Fluids* **23**, 063101 (2011).
- [14] M. Minale, Momentum transfer within a porous medium. I. Theoretical derivation of the momentum balance on the solid skeleton, *Phys. Fluids* **26**, 123101 (2014).
- [15] M. Minale, Momentum transfer within a porous medium. II. Stress boundary condition, *Phys. Fluids* **26**, 123102 (2014).
- [16] Y.-N. Young, Y. Mori, and M. J. Miksis, Slightly deformable Darcy drop in linear flows, *Phys. Rev. Fluids* **4**, 063601 (2019).
- [17] J. J. Feng and Y.-N. Young, Boundary conditions at a gel-fluid interface, *Phys. Rev. Fluids* **5**, 124304 (2020).
- [18] L. Li, J. Zhang, Z. Xu, Y.-N. Young, J. J. Feng, and P. Yue, An arbitrary Lagrangian-Eulerian method for simulating interfacial dynamics between a hydrogel and a fluid, *J. Comput. Phys.* **451**, 110851 (2022).
- [19] S. R. de Groot and P. Mazur, *Non-Equilibrium Thermodynamics* (North-Holland Publishing Co., Amsterdam/London, 1969).
- [20] C. Neto, D. R. Evans, E. Bonaccorso, H.-J. Butt, and V. S. J. Craig, Boundary slip in Newtonian liquids: A review of experimental studies, *Rep. Prog. Phys.* **68**, 2859 (2005).
- [21] P. Gao and J. J. Feng, Enhanced slip on a patterned substrate due to depinning of contact line, *Phys. Fluids* **21**, 102102 (2009).
- [22] S. K. Gupte and S. G. Advani, Flow near the permeable boundary of a porous medium: An experimental investigation using LDA, *Exp. Fluids* **22**, 408 (1997).
- [23] A. Goharzadeh, A. Khalili, and B. B. Jørgensen, Transition layer thickness at a fluid-porous interface, *Phys. Fluids* **17**, 057102 (2005).
- [24] J. K. Arthur, D. W. Ruth, and M. F. Tachie, PIV measurements of flow through a model porous medium with varying boundary conditions, *J. Fluid Mech.* **629**, 343 (2009).
- [25] A. Chakrabarti and M. K. Chaudhury, Direct measurement of the surface tension of a soft elastic hydrogel: Exploration of elastocapillary instability in adhesion, *Langmuir* **29**, 6926 (2013).
- [26] Y. A. Meier, K. Zhang, N. D. Spencer, and R. Simic, Linking friction and surface properties of hydrogels molded against materials of different surface energies, *Langmuir* **35**, 15805 (2019).
- [27] E. K. Hobbie, S. Lin-Gibson, and S. Kumar, Non-Brownian Microrheology of a Fluid-Gel Interface, *Phys. Rev. Lett.* **100**, 076001 (2008).
- [28] V. Gkanis and S. Kumar, Stability of pressure driven creeping flows in channels lined with a nonlinear elastic solid, *J. Fluid Mech.* **524**, 357 (2005).

- [29] R. Patne and V. Shankar, Stability of flow through deformable channels and tubes: implications of consistent formulation, *J. Fluid Mech.* **860**, 837 (2019).
- [30] V. Kumaran, Stability and the transition to turbulence in the flow through conduits with compliant walls, *J. Fluid Mech.* **924**, P1 (2021).
- [31] M. Pourjafar, S. Bazargan, and K. Sadeghy, Linear stability analysis of time-dependent fluids in plane Couette flow past a poroelastic layer, *J. Non-Newtonian Fluid Mech.* **266**, 1 (2019).
- [32] D. Arndt, W. Bangerth, B. Blais, M. Fehling, R. Gassmöller, T. Heister, L. Heltai, U. Köcher, M. Kronbichler, M. Maier, P. Munch, J.-P. Pelteret, S. Proell, K. Simon, B. Turcksin, D. Wells, and J. Zhang, The deal.II library, Version 9.3, *J. Num. Math.* **29**, 171 (2021).